remote sensing

MDPI

Article

Land Cover Mapping in East China for Enhancing High-Resolution Weather Simulation Models

Bingxin Ma [1], Yang Shao [2], Hequn Yang [1], Yiwen Lu [1], Yanqing Gao [1], Xinyao Wang [1], Ying Xie [1] and Xiaofeng Wang [1,*]

[1] Shanghai Meteorological Service, Shanghai 200030, China; mabx@simets.cn (B.M.); 19113020012@fudan.edu.cn (H.Y.); luyiwen164724@cma.cn (Y.L.); gaoyq@simets.cn (Y.G.); wangxy@simets.cn (X.W.); xiey@shnwp.org (Y.X.)

[2] Virginia Tech, Geography Department, College of Natural Resources and Environment, Blacksburg, VA 24061, USA; yshao@vt.edu

* Correspondence: wangxf@typhoon.org.cn; Tel.: +86-189-1820-6285

Abstract: This study was designed to develop a 30 m resolution land cover dataset to improve the performance of regional weather forecasting models in East China. A 10-class land cover mapping scheme was established, reflecting East China's diverse landscape characteristics and incorporating a new category for plastic greenhouses. Plastic greenhouses are key to understanding surface heterogeneity in agricultural regions, as they can significantly impact local climate conditions, such as heat flux and evapotranspiration, yet they are often not represented in conventional land cover classifications. This is mainly due to the lack of high-resolution datasets capable of detecting these small yet impactful features. For the six-province study area, we selected and processed Landsat 8 imagery from 2015–2018, filtering for cloud cover. Complementary datasets, such as digital elevation models (DEM) and nighttime lighting data, were integrated to enrich the inputs for the Random Forest classification. A comprehensive training dataset was compiled to support Random Forest training and classification accuracy. We developed an automated workflow to manage the data processing, including satellite image selection, preprocessing, classification, and image mosaicking, thereby ensuring the system's practicality and facilitating future updates. We included three Weather Research and Forecasting (WRF) model experiments in this study to highlight the impact of our land cover maps on daytime and nighttime temperature predictions. The resulting regional land cover dataset achieved an overall accuracy of 83.2% and a Kappa coefficient of 0.81. These accuracy statistics are higher than existing national and global datasets. The model results suggest that the newly developed land cover, combined with a mosaic option in the Unified Noah scheme in WRF, provided the best overall performance for both daytime and nighttime temperature predictions. In addition to supporting the WRF model, our land cover map products, with a planned 3–5-year update schedule, could serve as a valuable data source for ecological assessments in the East China region, informing environmental policy and promoting sustainability.

Keywords: land cover mapping; random forest; accuracy assessment; plastic greenhouses; East China

Citation: Ma, B.; Shao, Y.; Yang, H.; Lu, Y.; Gao, Y.; Wang, X.; Xie, Y.; Wang, X. Land Cover Mapping in East China for Enhancing High-Resolution Weather Simulation Models. *Remote Sens.* **2024**, *16*, 3759. https://doi.org/10.3390/rs16203759

Academic Editors: Silvia Liberata Ullo and Li Zhang

Received: 24 August 2024
Revised: 8 October 2024
Accepted: 9 October 2024
Published: 10 October 2024

1. Introduction

Accurate land cover mapping plays a crucial role in improving the performance of weather simulation models, such as the Weather Research and Forecasting (WRF) model. Land cover maps, used as inputs for surface characteristics in numerical models, play a critical role in influencing processes ranging from evapotranspiration to heat flux [1,2]. These processes, in turn, affect broader climate dynamics, making accurate land cover data critical for reliable meteorological simulations and predictions [3,4].

Changes in land use and land cover reflect the impact of human activities on terrestrial ecosystems, with far-reaching implications for global climate systems and biogeochemical

cycles [5–7]. As a result, land cover mapping has become a central focus of research related to global environmental changes and sustainable futures. Numerous studies have utilized remote sensing data to produce land cover products with varying spatial and temporal resolutions from localized regions to global scales [8–11].

However, inaccuracies in land cover datasets can distort weather simulations, leading to errors in the representation of weather patterns, temperature gradients, and precipitation predictions. This highlights the importance of continuously updating and integrating the WRF model with the most current and detailed land cover information to ensure more accurate simulations and forecasts [12].

The East China region is characterized by complex terrains, dense river networks, numerous lakes, and concentrated mega-cities, mostly located along the coast and rivers. Interactions between urban heat islands, sea (lake), and land breezes are intricate. Coastal city sea breezes and urban heat islands can amplify convective precipitation. Studies have shown that these interactions can enhance low-level convergence and updraft motions at the sea breeze front, leading to increased convective cloud formation and precipitation [13]. Although the basic WRF regional model offers multiple underlying surface datasets like AVHRR (1 km)- and MODIS (500 m)-derived land cover products to choose from, most of these datasets date back to 2010 or earlier. They suffer from a lack of spatial details, varying accuracies, and a failure to reflect land use changes due to rapid economic development in East China. Recently, there has been a surge in high-resolution global land cover products, with resolutions as detailed as 30 m or even finer. GlobeLand30, for instance, offers land cover datasets for 2000 to 2020 at a 30 m resolution [10], while ESRI boasts a 10 m resolution global land cover data using Seninel-2 imagery [14]. However, these global products exhibit varying mapping accuracy across different regions [15], and their classification systems might not align seamlessly with WRF model requirements. Given these challenges, there is a pressing demand for an updated, high-resolution land surface data product tailored to East China's unique topography and urban dynamics, thereby enhancing regional models for the region.

Regional land cover mapping for terrain-biologically complex ecosystems presents significant challenges, mainly due to phenology-induced errors and high within-class spectral variability [16,17]. Seasonal changes in plants' growth and development often introduce errors in the mapping process. The availability of cloud-free satellite imagery within a selected mapping window (e.g., growing season) may not be ideal for certain study regions, complicating the temporal selection of satellite passes [18]. Moreover, acquiring a substantial amount of training data points to accurately represent the spectral characteristics of mapping classes is particularly important for various classification algorithms [19]. It has been emphasized that the quality and comprehensiveness of training data can outweigh the importance of the chosen classification algorithms [20]. With the advent of machine learning, tools like the Random Forest, support vector machine, and various neural network-based methodologies have become accessible through open-source platforms such as scikit-learn in Python and the Caret library in the R environment. However, the main challenge in regional land cover mapping is not merely about algorithmic choices but in developing a comprehensive framework that seamlessly combines quality training data, appropriate imagery selection, and robust classification methods to address the intricate dynamics of complex ecosystems.

In this study, our primary aim was to develop a 30 m regional land cover mapping workflow for East China tailored to support high-resolution (km) WRF simulations and predictions. It is desirable to have an in-house, automated land cover mapping system that allows for easy expansion of mapping classes and the capability to rerun the mapping process every three years. Central to our workflow was the emphasis on developing high-quality training data, complemented by a careful selection of remote sensing and ancillary datasets. We also conducted a detailed, pixel-wise accuracy assessment and benchmarked our mapping accuracy against multiple global land cover products. A particularly compelling application of our refined land cover map is its assimilation into the

WRF model. For the scope of this investigation, we focused on its influence on urban heat wave predictions. This enhanced capability could potentially improve our understanding and prediction of localized climate patterns within East China.

2. Study Area

The East China region, stretching along China's eastern coast from 113°6′E to 122°6′E longitude and 23°4′N to 38°45′N latitude, encompasses six provinces (Shandong, Jiangsu, Zhejiang, Anhui, Jiangxi, Fujian) and Shanghai (Figure 1), spanning approximately 2160.6 km north–south and 1156.6 km east–west, totaling 795,740 square kilometers. It is characterized by plains, basins, and hills, with Jiangsu dominated by plains (over 70%), Shandong a mix of plains (55%) and mountains/hills (29%), Anhui's diverse terrain (Huai River Plain, Jianghuai Plateau, Western Anhui Hills, Yangtze River Area, Southern Anhui Hills), Shanghai's alluvial plain, Zhejiang's hills/mountains/basins (70.4%), Jiangxi's hills/mountains with basins/valleys, and Fujian's mountainous terrain (over 80%). This region's rapid economic growth has fueled infrastructure development, land use changes, and urbanization, positioning it as one of China's most dynamic economic and urbanizing areas. Located at the land–sea convergence and northern–southern climate transition, East China experiences a climate divided by the Huai River: temperate monsoon north and subtropical monsoon south, nurturing a rich landscape, ecosystem, complex surface features, dense river networks, numerous lakes, and coastal/riverine cities. Land cover changes here are influenced by both natural and socio-economic factors, with the latter increasingly dominant in recent decades [21].

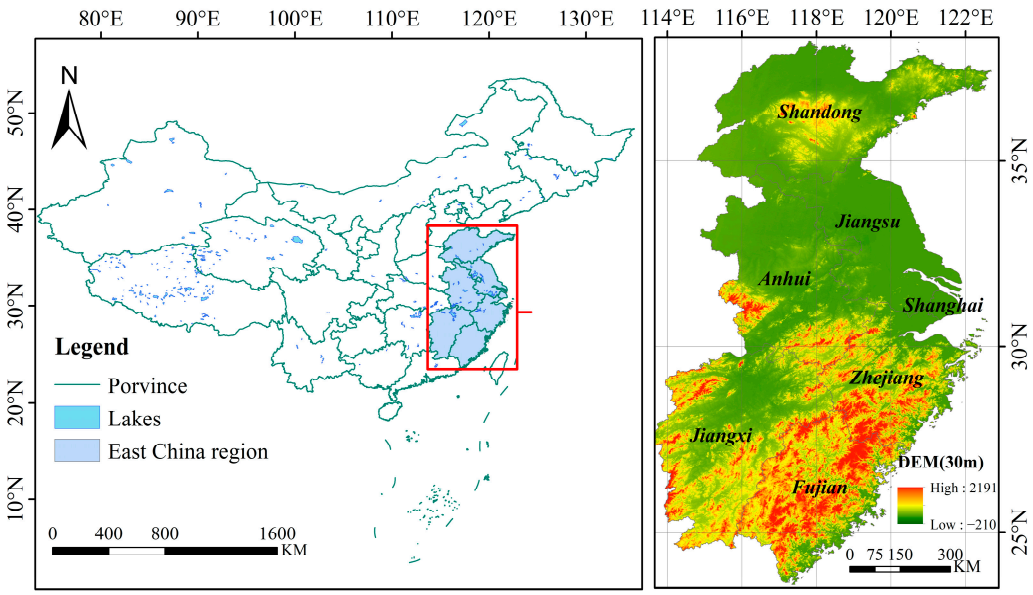

Figure 1. Location map of the six provinces in East China as the study area.

3. Materials and Methods

As depicted in the flowchart (Figure 2), the process is divided into three main sections. The first section focuses on pre-classification processing, encompassing data preprocessing, the design of the classification system, and the construction of a sample database. The second section pertains to the generation of land cover classification products, which involves setting classifier parameters, model training and cross-validation, accuracy assessment utilizing independent and randomly selected samples, and correction of data products. The third section concerns WRF numerical simulation, encompassing the parameterization of land cover products (including adaptation to the Mosaic scheme), the design of comparative experiments, and their subsequent evaluation.

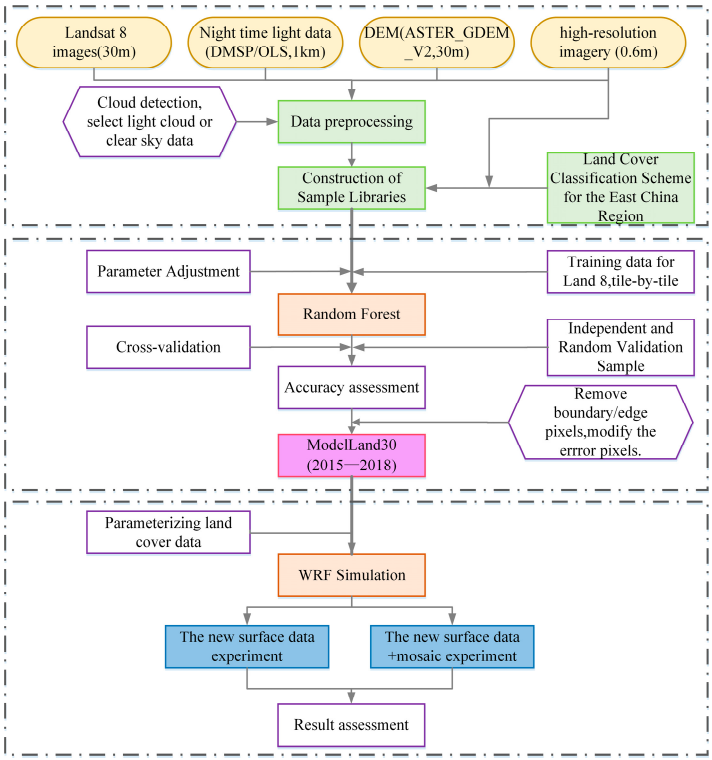

Figure 2. The flowchart of Land cover mapping in East China and experiment for WRF Simulation.

3.1. Data

We downloaded the Landsat-8 satellite, 2015 to 2018, from the United States Geological Survey (USGS) website, accessible at https://glovis.usgs.gov/ (accessed on 3 September 2018). This Landsat-8 imagery served as the primary input for land cover mapping. From the Landsat data spanning 2015–2018, a total of 72 images (paths 117–123, rows 33–44) covering the study area were selected (Figure 3). Factors considered included percent cloud cover (i.e., <10%) and relatively consistent vegetation phenology. Table 1 shows all imagery used for image classification, with 63% of the images corresponding to the spring season.

Our second major dataset comprised very high-resolution imagery (0.6 m) for all study provinces. These images are derived from TianDitu, a renowned mapping service in China, and supplemented by aerial photography from local government agencies. We implemented a tile-based hierarchical download process, followed by an image mosaic, to build seamless reference imagery for our study area. This high-resolution, seamless imagery served as an important reference for the training data selection and validation stages of our project. Additionally, we obtained a 30 m DEM dataset, ASTER_GDEM_V2, to provide an orographical context. Nighttime light data from DMSP/OLS (2013, 1 km) was also integrated. After resampling this data, it was used as an input band for the Random Forest model, primarily providing additional information about urban patterns; some typical images are shown in Figure 4.

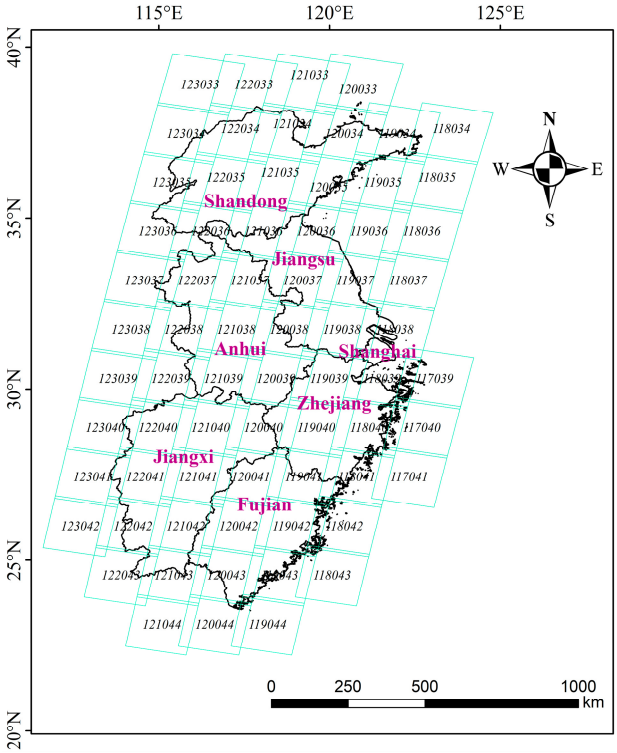

Figure 3. Landsat scenes utilized in this study, including row and path IDs.

Table 1. Specific image acquisition months for Landsat images used in this study. Most images are from the growing season.

Provinces	Landsat Image Acquisition Time (Month)
Anhui	March 2016, April 2018
Fujian	February 2017, October 2017, March 2018
Jiangsu	August 2015, October 2015, March 2016, May 2017
Jiangxi	October 2015, March 2016, September 2016, February 2018, April 2018
Shandong	October 2015, May 2017, September 2017, April 2018
Shanghai	August 2015
Zhejiang	August 2015, March 2016, February 2017, November 2017, March 2018

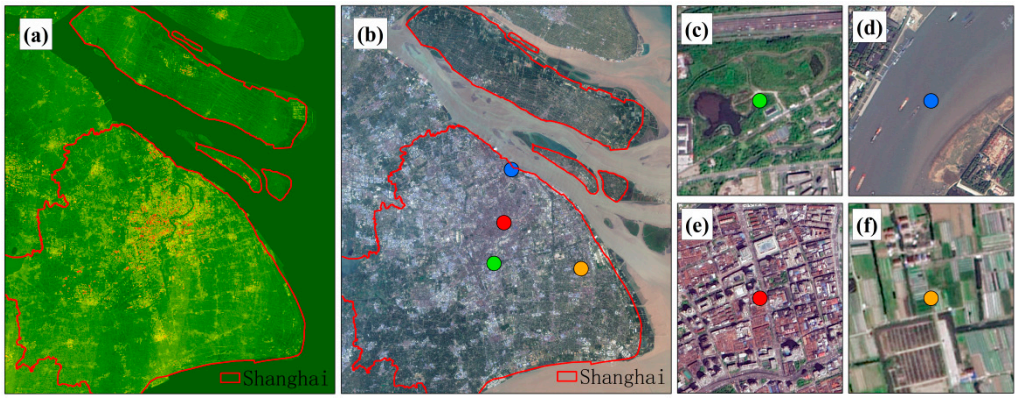

Figure 4. Some typical data used in Random Forest. (**a**) 30 m DEM dataset; (**b**) high-resolution imagery (0.6 m); with specific identification on the imagery (**b**) as follows: (**c**) Grasslands and Forest lands (marked by green dot); (**d**) Water bodies (marked by blue dot); (**e**) Urban (marked by red dot); (**f**) Croplands and Plastic greenhouses (marked by orange dot).

3.2. Land Cover Classification Scheme for the East China Region

A diverse array of land cover classification schemes exists, and the choice among them depends on the specific application. For example, the Intergovernmental Panel on Climate Change (IPCC) has provided guidelines for categorizing land cover types primarily in the context of greenhouse gas inventories. The broad land cover scheme mainly includes forest lands, croplands, grasslands, wetlands, settlements, and other lands. For weather numerical modeling, the International Geosphere-Biosphere Programme (IGBP) land cover classification system is a widely used scheme. The IGBP classification scheme includes more detailed land cover classes such as evergreen needleleaf forests, evergreen broadleaf forests, and deciduous needleleaf forests, among others. Guided by these foundational schemes [22,23], we developed a two-level classification system tailored to enhance high-resolution WRF modeling. The level-1 classification includes 10 primary land cover categories: urban and built-up lands, croplands, grasslands, forest lands, wetlands, water bodies, bare lands, plastic greenhouses, shrublands, and clouds, all detailed in Table 2. Notably, considering the prevalent spread of plastic greenhouses in North East China, we integrated a distinct category to represent these regional characteristics. Meanwhile, the level-2 classification subdivides forests and shrublands into specific vegetation types in alignment with IGBP standards. For the scope of this study, we focused on the level-1 classification.

Table 2. The land cover classification scheme used for East China land cover mapping. The definition of land cover categories follows those from the IGBP classification scheme.

Land Cover (Code)	Definition
Urban and built-up lands (1)	Any natural or artificial surface that prevents water from directly penetrating into the soil, mainly consisting of transportation land, building land, industrial and mining land, and rooftops within urban areas.
Croplands (2)	Land used for planting crops, including paddy fields, irrigated dry land, rainfed dry land, vegetable plots, pasture lands mainly for crops interspersed with fruit trees and other economic trees, as well as tea plantations, coffee plantations, and other economic shrub planting areas.
Grasslands (3)	Covered by herbaceous vegetation, with forest and shrub coverage less than 10%, including grasslands, meadows, urban grasslands, etc.
Forest lands (4)	Land covered with trees and a canopy cover of more than 30%, including deciduous broadleaf forest, evergreen broadleaf forest, deciduous, coniferous forest, evergreen coniferous forest, mixed forest, as well as sparse forest land with a canopy cover of 10% to 30%.
Wetlands (5)	A transitional zone between land and water bodies, often or perennially covered with shallow standing water (freshwater, brackish water, or saltwater) or overly moist soil, predominantly growing hydrophytic or hygrophytic herbaceous or woody plants. Includes inland marshes, lake marshes, river floodplain wetlands, forest/shrub wetlands, peat bogs, mangroves, salt marshes, etc.
Water bodies (6)	Areas covered by liquid water, including rivers, lakes, reservoirs, ponds, etc.
Bare lands (7)	Natural covered land with vegetation cover less than 10%, including bare soil, bare rocks, saline-alkali soil, desert, sandy land, gravel land, etc.
Plastic greenhouses (8)	Agricultural land used for vegetable cultivation utilizing facilities such as greenhouses and sheds.
Shrublands (9)	Land covered with shrubs and a shrub coverage greater than 30%, including mountain shrubland, deciduous and evergreen shrubland, as well as desert shrubland with coverage greater than 10% in desert areas.
Cloud (unclassified) (10)	Areas covered by clouds in satellite imagery, not classified into any specific land cover type due to obscuration.

3.3. Image Classification

Using high-resolution (0.6 m) seamless mosaic imagery as a reference, we manually selected training samples for land cover classes of interest. The training polygons were chosen to be spatially distributed across each Landsat scene to ensure spectral represen-

tativeness. Over 6000 training polygons and 100,000 sample points were collected, with particular emphasis on fine labeling of easily confused areas in suburban or urban–rural interface settings. In addition, we selected an independent and random validation sample (over 400 polygons, 40,000 samples) to evaluate the classification results. The distribution of the two types of samples is shown in Figure 5.

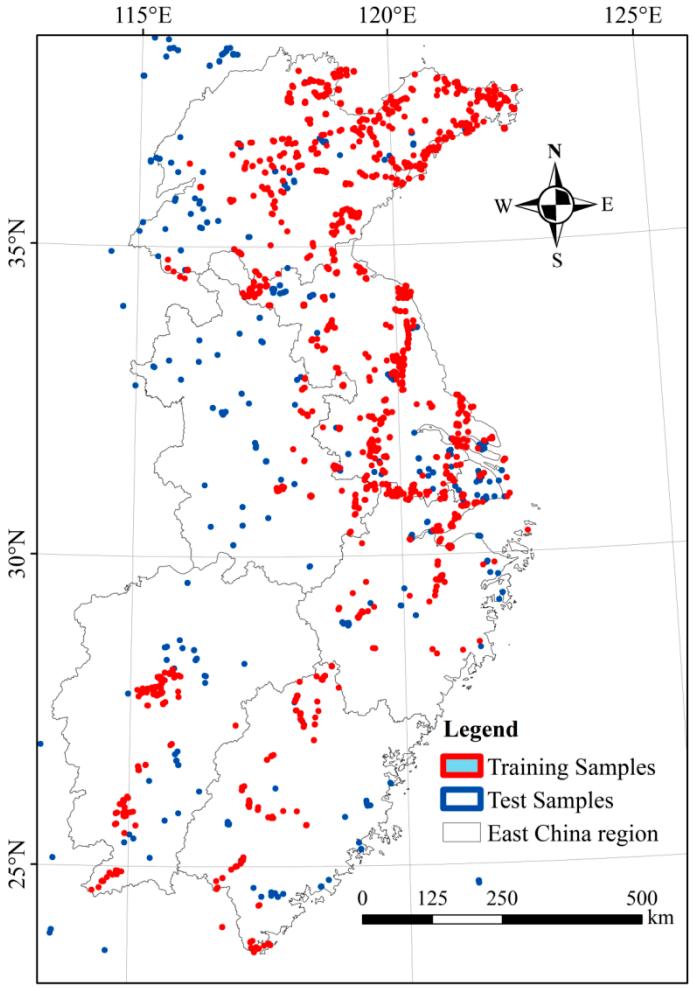

Figure 5. The distribution of the training dataset and the testing dataset.

This study utilized Landsat8 multispectral bands 2–7 as input data. Together with nighttime light data and DEM data, there were a total of 8 input bands. For optimal land cover mapping, we assessed several machine learning algorithms, including Random Forest (RF), Support Vector Machines (SVM), and a three-layer multilayer perceptron neural network. These algorithms have been routinely used in the land cover mapping domain [17,19]. For model training and validation, we employed the Caret package [24] within the R environment. The caret package enabled us to automatically select the best algorithm, in this case Random Forest, based on overall accuracy using a standard cross-validation approach.

We conducted algorithm training for all 72 images, treating each image as an independent analytical region for image classification. For example, using Landsat scene ID 121038, only training pixels within this scene were used to develop a scene-specific classifier. This approach was designed to mitigate challenges arising from phenological differences caused by varying image acquisition times. Upon training, we applied the classification algorithms to our validation sample, yielding key performance metrics such as overall accuracy, precision, recall, and the F1 score. The F1 score is calculated as the harmonic mean of precision and recall, with values ranging from 0 to 1, where 1 indicates better

performance [25]. After a detailed analysis of these metrics, we selected the RF algorithm for our primary classification due to its robust performance and minimal parameter tuning requirements. With the RF classifiers trained, we applied them across our study area, generating a comprehensive 10-class land cover map product.

3.4. WRF Modelling Using New Land Cover Data

The Advanced Research version of the Weather Research and Forecasting (WRF-ARW) model version 4 [26], developed by the National Center for Atmospheric Research (NCAR), was used to conduct the numerical simulations. The model setup uses a single-layer nesting with a horizontal grid spacing of 1 km and horizontal grid points of 559 × 505. There are 51 vertical layers, with the model top pressure set at 50 hPa. The physical parameterizations selected were the Thompson microphysics scheme [27], the rapid radiative transfer model (RRTM) longwave radiation scheme [28], the Dudhia shortwave radiation scheme [29], the Yonsei University (YSU) planetary boundary layer scheme [30], and the Unified Noah land surface scheme [31]. The cumulus convection parameterization scheme was turned off because deep convection can be explicitly simulated at a kilometer-scale resolution. The 6-hourly, 0.25° × 0.25° National Centers for Environmental Prediction (NCEP) Final Operational Global Analysis data (FNL) was used for the initial and lateral boundary conditions. The simulation period was from 0800 local time (LT) on 12 August 2020, to 0800 LT on 17 August 2020. To avoid the spin-up problem, the first 24 h simulation was discarded. To evaluate the simulation capability of the new surface data for the heatwave process, three sets of experiments were conducted. The first experiment used the default WRF surface data derived from an old version of MODIS (2011–2013) land cover map products. The second experiment used the new surface data derived from our newly developed land cover map products ModelLand30 (2015–2018), and the third experiment was based on the second experiment but with the mosaic option in the Unified Noah scheme turned on. The aim of the third experiment was to test the influence of the subgrid-scale surface heterogeneity. Due to the limitation of computing resources, it is difficult for the grid spacing of current weather models to reach a meter-scale resolution (e.g., 30 m resolution). However, surface characteristics with a resolution below the grid spacing (e.g., 1 km) can be used as subgrid-scale information to influence grid-scale meteorological elements. The mosaic scheme, the Unified Noah scheme, can represent the subgrid-scale surface characteristics [32].

4. Results

4.1. Land Cover Distribution

The Landsat-derived 10-class land cover map for East China is depicted in Figure 6. The map is named ModelLand30 (2015–2018). The study region exhibited a distinct contrast between its northern and southern parts. The northern area was predominantly characterized by vast stretches of croplands, while the southern region was distinguished by extensive forest lands. Forest lands were the dominant land cover type in the study region, covering nearly 330,000 square kilometers. Croplands were the second most common type, mainly distributed in the central and northern parts of East China, with an area of nearly 250,000 square kilometers. Urban and built-up lands covered more than 90,000 square kilometers, notably forming a Z-shaped belt in the Yangtze River Delta region. Due to the coastal location and large inland lakes, such as Taihu Lake and Poyang Lake, water bodies also covered a significant area. Other types of land cover, such as grasslands, wetlands, and shrublands, were relatively smaller in area and more sparsely distributed. Plastic greenhouses covered 8700 square kilometers, mainly in Shandong and northern Jiangsu. Figure 7 shows the distribution of the four main land cover types (urban, forest lands, croplands, and grasslands) across different provinces within the study area. The proportion of these four cover types in each province exceeded 80%, except for Shandong (75.82%). Among them, Fujian, Jiangxi, and Zhejiang were dominated by forest lands, accounting for 77.72%, 60.69%, and 66.82%, respectively; Anhui, Jiangsu, and Shandong were dominated

by croplands, accounting for 43.31%, 57.06%, and 38.11%, respectively; and Shanghai was mainly composed of urban built-up lands, with the urban area accounting for 42.19% (Table 3).

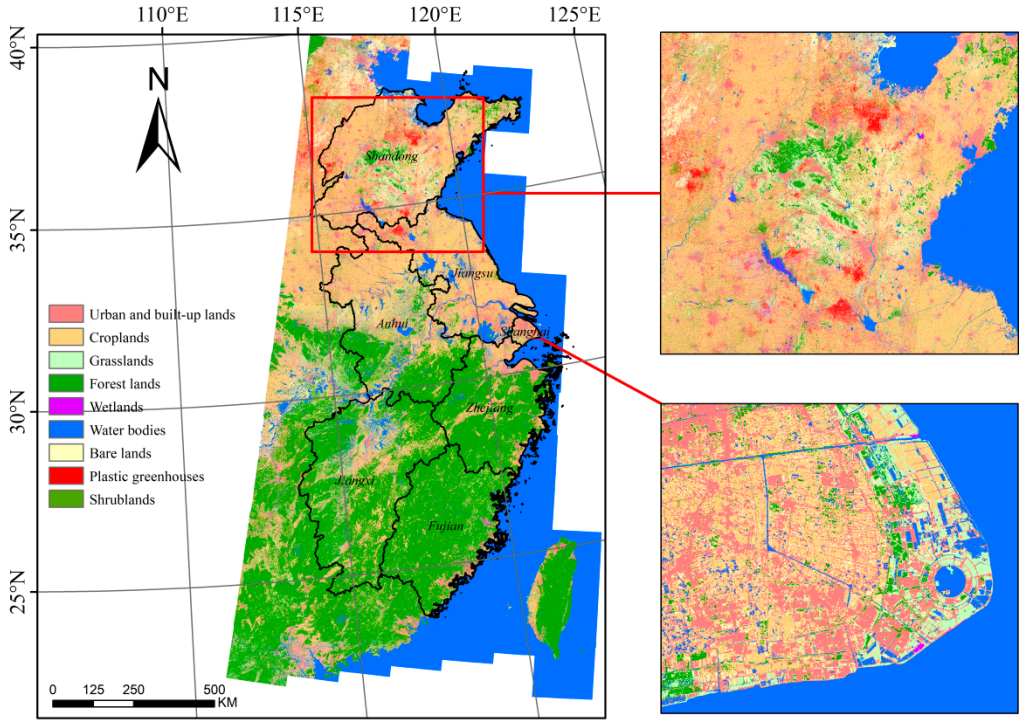

Figure 6. 30 m Land cover map product for East China.

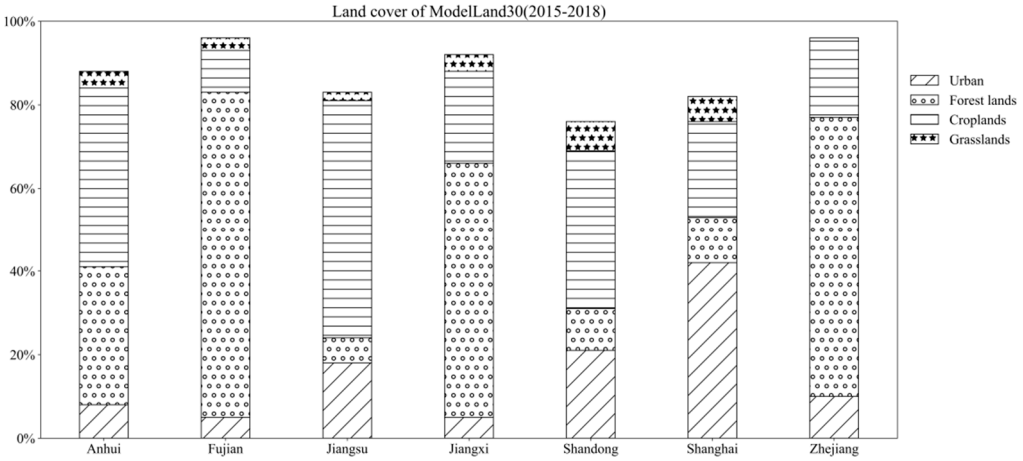

Figure 7. Distribution of major land cover types across six study provinces.

Table 3. Percentage of different land cover types across six study provinces.

Class	Percentage of Different Land Cover Types (%)						
	Anhui	**Fujian**	**Jiangsu**	**Jiangxi**	**Shandong**	**Shanghai**	**Zhejiang**
Urban	8.29	4.92	17.94	5.28	21.28	42.19 [1]	9.96
Croplands	43.31 [1]	10.28	57.06 [1]	22.42	38.11 [1]	22.95	18.69
Grasslands	3.79	2.70	2.49	3.97	6.85	6.27	0.30
Forest lands	33.03	77.72 [1]	5.65	60.69 [1]	9.58	11.38	66.82 [1]

Table 3. *Cont.*

Class	Percentage of Different Land Cover Types (%)						
	Anhui	**Fujian**	**Jiangsu**	**Jiangxi**	**Shandong**	**Shanghai**	**Zhejiang**
Wetlands	1.17	0.46	0.66	0.05	1.03	0.30	0.03
Water bodies	6.97	1.41	12.34	4.95	3.85	5.40	2.71
Bare lands	3.00	2.45	2.53	2.57	14.74	11.44	1.48
Plastic greenhouses	0.44	0.05	1.31	0.06	4.23	0.00	0.01
Shrublands	0.00	0.01	0.00	0.00	0.34	0.06	0.00

[1] The type with the highest proportion has a footer with red font.

4.2. Accuracy Assessment

The cross-validation accuracy statistics for all land cover types are presented using a standard confusing matrix (Table 4). The overall accuracy was 83.2%, and the Kappa coefficient [33] was 0.81. The producer accuracies for wetlands, water bodies, and plastic greenhouses were 0.96, 0.92, and 0.92, respectively, indicating that a large majority of all wetlands, water bodies, and plastic greenhouses pixels had been correctly identified. The classifications of urban areas, bare lands, and shrublands also performed well, with producer accuracies of 0.87, 0.82, and 0.80, respectively. Grasslands and forest lands had lower producer accuracies of 0.77 and 0.72, with some misclassifications occurring, mainly involving grasslands being misclassified as shrublands. Croplands had the lowest producer accuracy of only 0.66, reflecting significant challenges encountered during the classification process, where bare croplands are often misclassified as urban or grasslands.

Table 4. Accuracy assessment for land cover classification using RF algorithm.

Class	Urban	Cropland	Grassland	Forest	Wetland	Water	Bare Land	Plastic Greenhouses	Shrubland	User Acc.
Urban	**7308** [1]	246	6	122	88	41	156	27	40	0.91
Croplands	67	**2555** [1]	73	8	3	265	49	0	0	0.85
Grasslands	46	439	**2300** [1]	32	3	5	238	49	205	0.69
Forest lands	30	10	81	**3259** [1]	0	3	26	0	237	0.89
Wetlands	318	77	566	60	**3679** [1]	211	129	20	2	0.73
Water bodies	46	48	5	11	26	**6607** [1]	0	2	0	0.98
Bare lands	351	217	92	110	37	14	**4053** [1]	12	35	0.82
Plastic green-houses	124	204	15	73	0	2	5	**1547** [1]	0	0.79
Shrublands	584	51	45	585	0	0	24	18	**2045** [1]	0.61
Producer Acc.	0.82	0.66	0.72	0.77	0.96	0.92	0.87	0.92	0.80	

[1] The number of instances correctly predicted by the model has a footer with bold font.

Regarding user accuracy, water bodies and urban had user accuracies of 0.98 and 0.91, respectively. Forest lands, croplands, and bare lands had user accuracies of 0.89, 0.85, and 0.82, respectively, demonstrating reliable classification results for these categories. Plastic greenhouses and wetlands had user accuracies of 0.79 and 0.73, suggesting there is still room for improvement for these two classes. Grasslands and shrublands had the lowest user accuracies, at 0.69 and 0.61, respectively. The main reason for this is that grasslands can easily be confused with croplands and low-lying shrubbery. Overall, the table shows good classification performance for most land cover types, but there are some challenges in distinguishing plastic greenhouses, wetlands, grasslands, and shrublands from other classes. Notably, plastic greenhouses are currently not incorporated into existing classification systems. By conducting scenario experiments with these new categories in various contexts, we can facilitate their proper integration into future models.

We further calculated the F1 scores for all land cover categories and classified them into three levels (Table 5). The highest level of F1 scores (>0.9) encompassed water bodies, which possess unique spectral characteristics that minimize the likelihood of misclassification or omission. The F1 scores for urban areas, plastic greenhouses, bare lands, wetlands, and forest lands fell into the second level, with values of 0.86, 0.85, 0.84, 0.83, and 0.82, respectively. Among these, wetlands were prone to misclassification due to their spectral similarity to grasslands; 11.18% of all actual wetland samples were erroneously classified as grasslands, resulting in a recall rate of 73%. Croplands, grasslands, and shrublands had the lowest F1 scores, at 0.74, 0.71, and 0.69, respectively. Specifically, bare lands, due to their complex physical properties, could easily be confused with developing urban areas, abandoned croplands, and loose forest grasslands; 11.54% of all actual bare land samples were misclassified as either urban areas or croplands. Shrublands were prone to confusion with sparse trees and tall grasses in suburban areas and loose forests; 34.87% of all actual shrubland samples were misclassified as urban and forest lands, yielding a recall rate of only 61%.

Table 5. Accuracy assessment for land cover classification.

Class	TP [1]	FN [1]	FP [1]	TN [1]	Precision [1]	Recall	TNR [1]	F1 Score
Urban	7308	726	1566	30,467	0.82	0.91	0.95	0.86
Croplands	2555	465	1292	35,755	0.66	0.85	0.97	0.74
Grasslands	2300	1017	883	35,867	0.72	0.69	0.98	0.71
Forest lands	3259	387	1001	35,420	0.77	0.89	0.97	0.82
Wetlands	3679	1383	157	34,848	0.96	0.73	1.00	0.83
Water bodies	6607	138	541	32,781	0.92	0.98	0.98	0.95
Bare lands	4053	868	627	34,519	0.87	0.82	0.98	0.84
Plastic greenhouses	1547	423	128	37,969	0.92	0.79	1.00	0.85
Shrublands	2045	1307	519	36,196	0.80	0.61	0.99	0.69

[1] TP: true positive; FN: false negative; FP: false positive; TN: true negative; TNR: true negative rate.

4.3. Comparisons with Other Products

We compared our results with various land cover products developed at global and regional scales. These products were derived from different satellite sensors and employed a range of classification methods, each offering unique advantages in terms of resolution, accuracy, and temporal coverage (Table 6). For example, the GLC 2000 product, derived from SPOT4 data, used an unsupervised classification method and offered a resolution of 1 km, providing an overall accuracy of 68.6%. Similarly, the IGBP-DIS and UMD products, both based on AVHRR data, employed unsupervised and decision tree classification methods, respectively, with overall accuracies of 66.9% and 65.0%. The MCD12Q1 product, utilizing MODIS data, combined supervised classification, decision trees, and neural networks to achieve a higher overall accuracy of 74.8% at a 500 m resolution. Meanwhile, the GlobCover product, which integrates MERIS data with supervised and unsupervised classification techniques, offered a 300 m resolution and an overall accuracy of 67.5%. The CCI-LC product, combining data from MERIS and SPOT sensors, used an unsupervised classification approach to provide a 300 m resolution with a 74.1% overall accuracy. Among these, the GlobeLand30 product stood out with an 80.0% overall accuracy, derived from LANDSAT and HJ-1A/B data, utilizing pixel/object-based and knowledge rule classification methods at a 30 m resolution. These diverse products highlight the evolution and advancements in land cover mapping technologies and methodologies.

Table 6. Various land cover products available at different spatial resolutions and mapping accuracies.

Products	Overall Accuracy (%)	Sensor	Classification Method	Resolution	Year	References
IGBP-DIS	66.9	AVHRR	Unsupervised Classification	1 km	1992–1993	[34]
UMD	65.0	AVHRR	Unsupervised/Decision Tree Classification	1 km	1992–1993	[35]
GLC 2000	68.6	SPOT4	Unsupervised Classification	1 km	1999–2000	[36]
GlobCover	67.5	MERSI	Supervised/Unsupervised Classification	300 m	2009	[37]
CCI-LC	74.1	MERIS, SPOT	Unsupervised Classification	300 m	2008–2012	[23]
MCD12Q1	74.8	MODIS	Supervised Classification/Decision Tree/Neural Network	500 m	2013	[38]
GlobeLand30	80.0	LANDSAT, HJ-1A/B	Pixel/Object-based and Knowledge Rule Classification	30 m	2010, 2020	[39]

The following Table 7 presents a comparative analysis of land cover data across three different datasets: ModelLand30 (2015–2018), GlobeLand30 (2010), and MODIS (2013). As shown in Figure 8, urban areas exhibited an increase in coverage in ModelLand30 (2015–2018) compared to the earlier GlobeLand30 and MODIS data, indicating urban expansion over time. Croplands, which represented the largest land cover type in the MODIS dataset, showed a slightly lower proportion in ModelLand30 (2015–2018). Forest lands were mapped most extensively in ModelLand30 (2015–2018), which suggests either an increase in forest areas or improvements in mapping techniques. Wetlands and water bodies maintained consistent proportions across the datasets, while bare land coverage was significantly less in the GlobeLand30 dataset. Shrublands showed the least variation across the years, maintaining a minimal presence in the land cover composition of East China. This analysis highlights changes in land use and advancements in land cover mapping resolution and accuracy over the years.

Table 7. Comparison of Three Classification Results.

Class	GlobeLand30 (2010)		MODIS (2013)		ModelLand30 (2015–2018)	
	Area (km^2)	Proportion (%)	Area (km^2)	Proportion (%)	Area (km^2)	Proportion (%)
Urban	58,330.4	7.32	20,539.5	2.73	90,918.9	11.42
Croplands	384,160.9	48.24	386,304	51.31	248,857.7	31.25
Grasslands	32,970.8	4.14	75,582	10.04	29,177.4	3.66
Forest lands	279,741.1	35.13	244,495.5	32.47	332,869.8	41.79
Wetlands	4710.3	0.59	7913.75	1.05	4617.9	0.58
Water bodies	34,335.5	4.31	14,502	1.93	41,461.7	5.21
Bare lands	676.8	0.08	2228.75	0.30	39,316.8	4.94
Plastic greenhouse	NA	NA	NA	NA	8687.9	1.09
Shrublands	725.7	0.09	1194.75	0.16	538.7	0.07

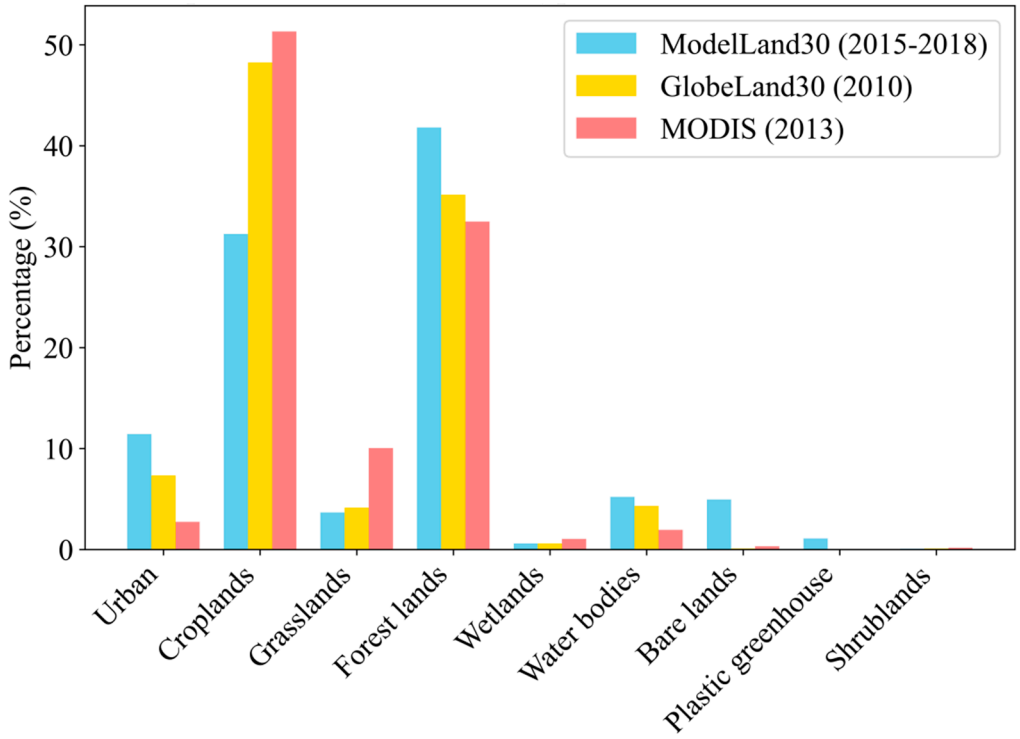

Figure 8. Comparison of landcover types across different datasets.

4.4. WRF Model Results

To compare the temperature simulation differences between day and night during a heatwave process, representative times were set at 1600 LT on 13 August 2020 (daytime) and 0200 LT on 14 August 2020 (nighttime). Figure 9 shows the differences between simulated and observed 2 m temperatures at 16:00 on 13 August and 02:00 on 14 August 2020. From Figure 9, it can be seen that the original surface data experiment showed a significant cold bias in nighttime temperatures. The new surface data experiment could better reduce this cold bias, but it introduced a noticeable warm bias in southern Jiangsu and northwestern Shanghai. The new surface data + mosaic experiment could reduce the warm bias introduced by the new surface data experiment. All three experiments showed a significant warm bias in simulating daytime temperatures in the central urban area of Shanghai. Specifically, the new surface data + mosaic experiment further reduced the warm bias compared to the new surface data experiment alone.

To statistically evaluate the impact of the new surface data on the quantitative forecast skill, Figure 10 shows the time series of the error (simulations minus observations) and the root mean square error (RMSE) of 2 m temperatures. Additionally, Table 8 shows the averaged root mean square error, mean error (ME), and mean absolute error (MAE) of the simulated 2 m temperature compared to surface stations from 0800 LT 13 to 0800 LT 17 August 2020. Evidently, the original surface data experiment underestimated the 2 m temperature, with the ME of −1.42 °C. Compared with the original surface data experiment, the new surface and new surface + mosaic experiments could reduce the cold bias, with the ME of −0.64 and −0.57 °C, respectively. The RMSE and MAE of the 2 m temperature from the new surface experiment were lower than those of the original surface data experiment, indicating that the application of the new surface data in the weather model could improve the 2 m temperature forecasting ability. Additionally, the new surface data + mosaic experiment had lower error values than the new surface data experiment due to the inclusion of subgrid-scale surface heterogeneity in the mosaic scheme [31].

Table 8. Statistical evaluation results of three simulated experiments.

Experiments	Averaged Root Mean Square Error (°C)	Mean Error (°C)	Mean Absolute Error (°C)
Original surface data	3.36	−1.42	1.99
New surface data	3.09	−0.64	1.47
New surface data + mosaic	3.01	−0.57	1.36

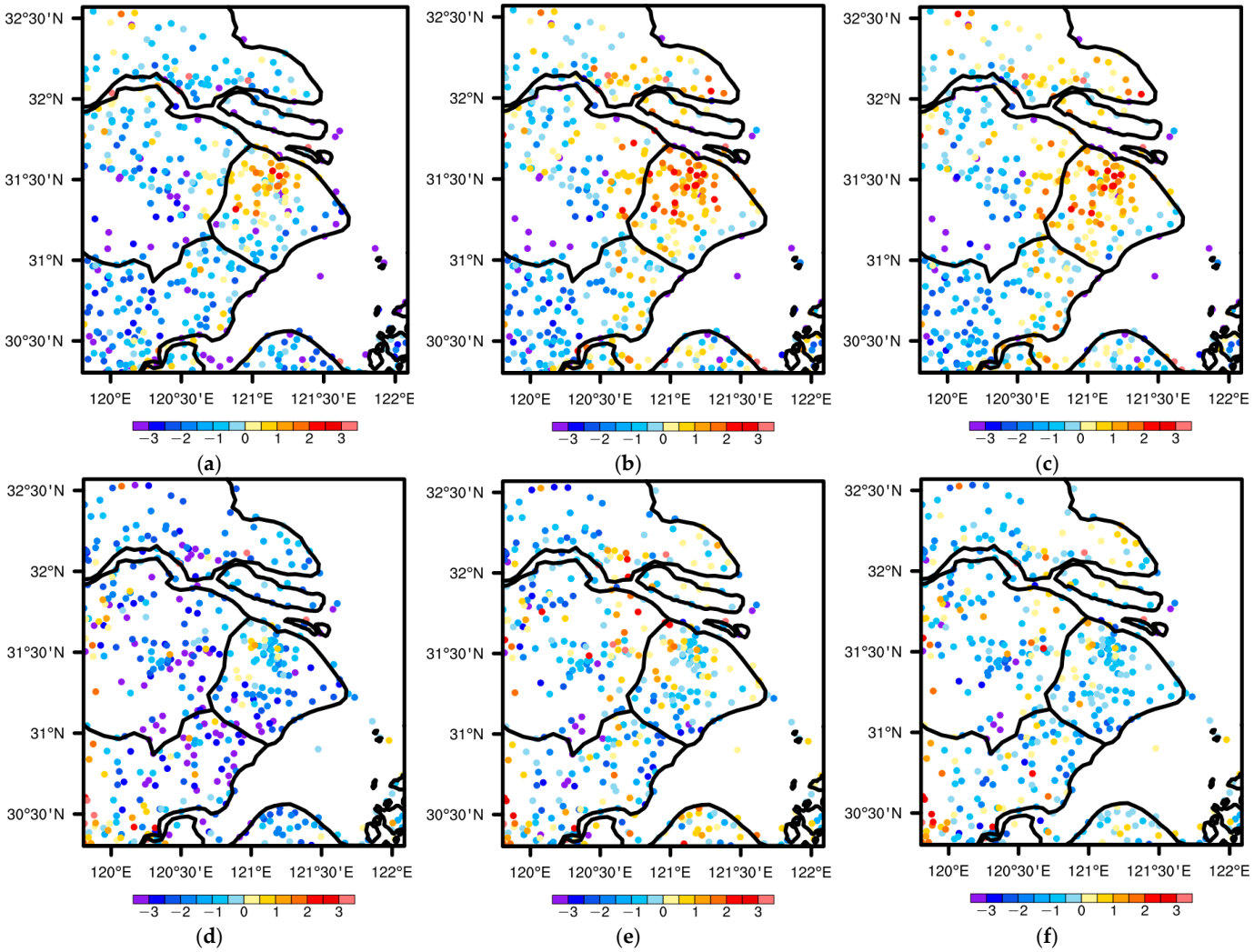

Figure 9. Difference between simulated and observed 2 m temperatures. (**a**–**c**) at 16:00 on 13 August 2020, and (**d**–**f**) at 02:00 on 14 August 2020 (shading, units: °C). (**a**,**d**) Original surface data, (**b**,**e**) New surface data, (**c**,**f**) New surface data + mosaic.

The reduction in cold bias and improvement of the 2 m temperature forecasting ability in the new surface data experiment may be attributed to the reasonable representation of the urban area. Compared with the original surface data experiment using the old version of the MODIS land cover dataset, the new surface data experiment using the ModelLand30 land cover dataset could better represent the urban heat effect, especially in the nighttime (Figure 7) due to the increase in urban area and proportion (Table 7).

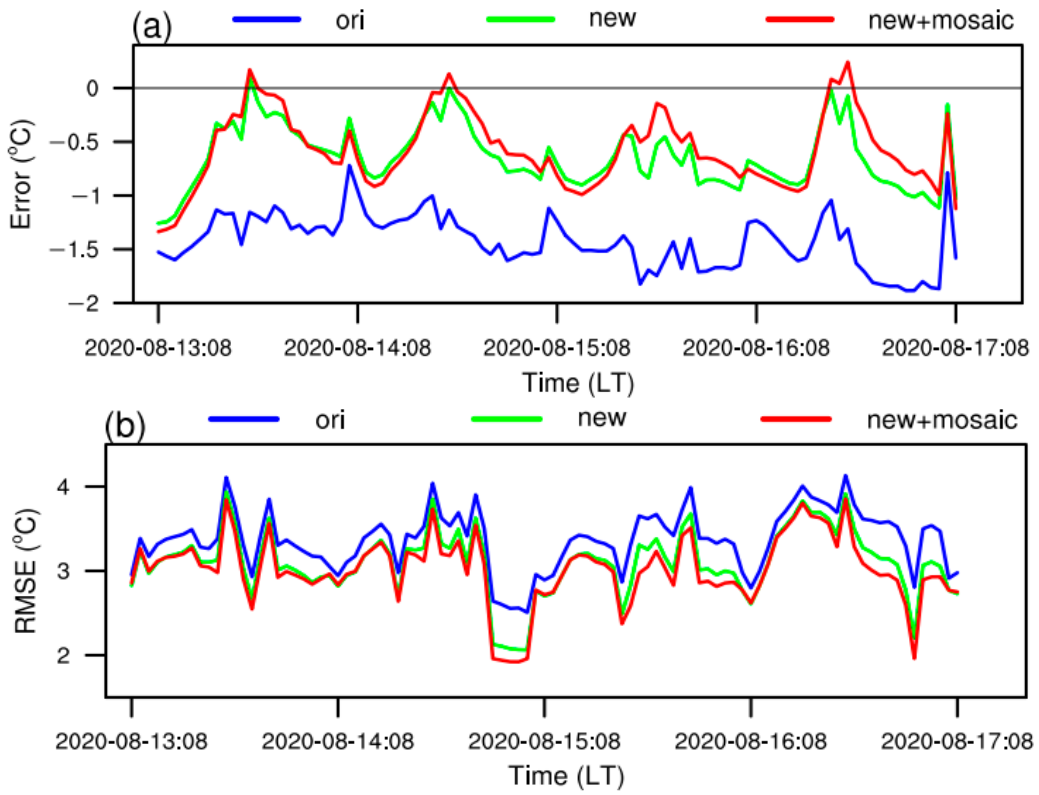

Figure 10. Time series of (**a**) the error and (**b**) the root mean square error of 2 m temperature.

5. Discussion

The development of a high-resolution (30 m) land cover dataset tailored to East China's diverse landscape is important for both meteorological modeling and environmental management. Existing national and global land cover datasets often fall short in spatial, temporal, and thematic accuracies needed to accurately represent regional surface characteristics, which can negatively impact meteorological modeling [22,35,40]. One of the primary motivations for developing this 30 m land cover map product is its application in enhancing the WRF model. Accurate land cover data are crucial for defining surface–atmosphere interactions, influencing processes such as evapotranspiration and heat flux [41,42]. This is particularly important for East China, where rapid urbanization and complex terrain significantly impact local climate dynamics. The primary advantage of developing an in-house land cover product, rather than relying on existing data, is the flexibility it provides in adjusting the classification scheme and update schedule. For example, we included plastic greenhouses as an additional land cover category due to their unique spectral characteristics and significant spatial coverage in the study region. However, current land surface schemes in the WRF model lack the descriptions of the physical process corresponding to the plastic greenhouses type; therefore, for the current WRF simulation, plastic greenhouses have been classified under the land cover type 'bare lands'. However, in future studies, we plan to represent plastic greenhouses using their specific surface parameters, such as albedo. This type will work when the physical processes related to the plastic greenhouse type are introduced into the land surface schemes.

Similar to other regional or national-scale land cover mapping tasks, the main challenges for successful land cover classification are associated with phenological variability and within-class spectral diversity [43]. By treating each Landsat image as an independent analytical region for classification, we mitigated errors caused by seasonal changes in vegetation, ensuring robust classification across different times and conditions [44]. The inclusion of a large and diverse training dataset further enhanced the model's ability to accurately classify various land cover types, as evidenced by high producer and user accura-

cies for important categories such as urban and forest lands. We also incorporated ancillary data, such as digital elevation models and nighttime lighting, into our land cover mapping. Among several machine learning algorithms evaluated, we found Random Forest to be the most appealing due to its performance and ease of implementation, particularly when using R's caret package with automatic parameter tuning and model selection [45].

Our regional land cover mapping effort achieved an overall accuracy of 83.2% and a Kappa coefficient of 0.81. A comparative analysis with existing land cover products highlights the advancements made by our dataset. For instance, our product's overall accuracy surpasses earlier datasets such as GLC 2000 (68.6%), IGBP-DIS (66.9%), and UMD (65.0%), as well as more recent products like GlobCover (67.5%) and CCI-LC (74.1%). GlobeLand30, which also offers high-resolution data, achieved an accuracy of 80.0%, slightly lower than our dataset. This comparison underscores the continuous improvement in land cover mapping technologies and the importance of incorporating local-specific classifications and high-resolution imagery. These results are expected because we used localized training data and the Random Forest algorithm, which is robust when high-quality training data is available.

By providing a more detailed and up-to-date land cover boundary layer, our dataset enables more precise regional weather simulations and predictions, particularly enhancing the WRF model's performance. For the scope of this study, we only included three WRF experiments to highlight daytime and nighttime temperature predictions using different land cover maps as input. For a future study, we plan to expand the number of WRF experiments to cover a wider range of meteorological variables and seasons. We intend to analyze precipitation patterns, wind speed, and humidity levels across different seasons to provide a comprehensive assessment of our land cover dataset's impact on weather modeling. Additionally, we aim to investigate the effects of land cover changes over time on climate variables to better understand long-term environmental trends.

Beyond meteorological applications, the high-resolution land cover dataset has broader implications for environmental policy and sustainable land management. By providing detailed and accurate information on land use changes, such as the expansion of urban areas and the distribution of plastic greenhouses, policymakers and planners can make more informed decisions. The automated workflow developed in this study ensures the practicality and scalability of the land cover mapping system, allowing for continuous monitoring and updates. Future refinements and integration of advanced machine learning algorithms could further enhance accuracy, improving weather forecasts and climate predictions for East China.

6. Conclusions

We developed regional land cover map products for East China to support high-resolution WRF modeling and prediction. A total of 72 Landsat8 images, combined with DEM and nighttime lighting data, were used to develop a 10-class land cover map. Focusing on the collection of high-quality training points and scene-specific RF classification, our regional mapping achieved an overall accuracy of 83.2% and a Kappa coefficient of 0.81, outperforming existing datasets. The automated workflow developed for this project ensures efficient data processing and future updates. Our three WRF model experiments demonstrated the improved performance of daytime and nighttime temperature predictions using new land cover maps.

Future studies will expand the range of WRF experiments to include various meteorological variables and seasons, further validating our dataset's impact on weather modeling. Additionally, our high-resolution land cover dataset holds significant potential for ecological assessments, environmental policy formulation, and sustainable land management in the East China region, providing a robust foundation for ongoing and future research.

Author Contributions: Conceptualization, X.W. (Xiaofeng Wang); Data curation, H.Y., Y.L. and X.W. (Xinyao Wang); Formal analysis, Y.G.; Methodology, B.M., Y.S. and X.W. (Xiaofeng Wang); Validation,

B.M., H.Y. and Y.L.; Writing—original draft, B.M.; Writing—review and editing, Y.S. and Y.X. All authors have read and agreed to the published version of the manuscript.

Funding: This research was funded by Natural Science Foundation of Shanghai (Grant No. 22ZR1456100) and the Shanghai Collaborative Innovation Special Foundation (Grant No. CXXT-2023-06).

Data Availability Statement: The data presented in this study are available on request from the corresponding author. The data are not publicly available due to privacy or ethical restrictions.

Conflicts of Interest: The authors declare no conflicts of interest.

References

1. Skamarock, W.C.; Klemp, J.B. A Time-Split Nonhydrostatic Atmospheric Model for Weather Research and Forecasting Applications. *J. Comput. Phys.* **2008**, *227*, 3465–3485. [CrossRef]
2. Dudhia, J. Coupling an Advanced Land Surface–Hydrology Model with the Penn State–NCAR MM5 Modeling System. Part I: Model Implementation and Sensitivity. *Mon. Weather Rev.* **2001**, *129*, 569–585. [CrossRef]
3. Bonan, G.B. The Land Surface Climatology of the NCAR Land Surface Model Coupled to the NCAR Community Climate Model. *J. Clim.* **1998**, *11*, 1307–1326. [CrossRef]
4. Pielke, R., Sr.; Pitman, A.; Niyogi, D.; Mahmood, R.; Mcalpine, C.; Hossain, F.; Klein Goldewijk, K.; Nair, U.; Betts, R.; Fall, S.; et al. Land Use/Land Cover Changes and Climate: Modeling Analysis and Observational Evidence. *Wiley Interdiscip. Rev. Clim. Change* **2011**, *2*, 828–850. [CrossRef]
5. Foley, J.; Defries, R.; Asner, G.; Barford, C.; Bonan, G.; Carpenter, S.; Chapin III, F.S.; Coe, M.; Daily, G.; Gibbs, H.; et al. Global Consequences of Land Use. *Science* **2005**, *309*, 570–574. [CrossRef]
6. Li, X. A review of the international researches on land use/land cover change. *J. Geogr. Sci.* **1996**, *51*, 553–558.
7. Zhao, P.; Fu, Y.; Zheng, L.; Feng, X.; Satyanarayana, B. Cart-Based Land Use/Cover Classification of Remote Sensing Images. *J. Remote Sens.* **2005**, *9*, 708–716.
8. George Grekousis, G.M.; Kavouras, M. An Overview of 21 Global and 43 Regional Land-Cover Mapping Products. *Int. J. Remote Sens.* **2015**, *36*, 5309–5335. [CrossRef]
9. Yu, L.; Wang, J.; Gong, P. Improving 30 m Global Land-Cover Map FROM-GLC with Time Series MODIS and Auxiliary Data Sets: A Segmentation-Based Approach. *Int. J. Remote Sens.* **2013**, *34*, 5851–5867. [CrossRef]
10. Chen, J.; Liao, A.; Chen, J.; Peng, S.; Chen, L.; Zhang, H. 30-Meter Global Land Cover Data Product- Globe Land30. *Geomat. World* **2017**, *24*, 1–8.
11. Chen, J.; Dowman, I.; Li, S.; Li, Z.; Madden, M.; Mills, J.; Paparoditis, N.; Rottensteiner, F.; Sester, M.; Toth, C.; et al. Information from Imagery: ISPRS Scientific Vision and Research Agenda. *ISPRS J. Photogramm. Remote Sens.* **2016**, *115*, 3–21. [CrossRef]
12. Tewari, M.; Chen, F.; Wang, W.; Dudhia, J.; LeMone, M.A.; Mitchell, K.; Ek, M.; Gayno, G.; Wegiel, J.; Cuenca, R. Implementation and Verification of the United NOAH Land Surface Model in the WRF Model. In Proceedings of the 84th American Meteorological Society (AMS) Annual Meeting—Combined Preprints, Seattle, WA, USA, 11–15 January 2004.
13. Fan, J.; Shen, S.; Erwin, D.H.; Sadler, P.M.; MacLeod, N.; Cheng, Q.; Hou, X.; Yang, J.; Wang, X.; Wang, Y.; et al. A High-Resolution Summary of Cambrian to Early Triassic Marine Invertebrate Biodiversity. *Science* **2020**, *367*, 272–277. [CrossRef] [PubMed]
14. Karra, K.; Kontgis, C.; Statman-Weil, Z.; Mazzariello, J.C.; Mathis, M.; Brumby, S.P. Global Land Use/Land Cover with Sentinel 2 and Deep Learning. In Proceedings of the 2021 IEEE International Geoscience and Remote Sensing Symposium IGARSS, Brussels, Belgium, 11–16 July 2021; pp. 4704–4707.
15. Venter, Z.S.; Barton, D.N.; Chakraborty, T.; Simensen, T.; Singh, G. Global 10 m Land Use Land Cover Datasets: A Comparison of Dynamic World, World Cover and Esri Land Cover. *Remote Sens.* **2022**, *14*, 4101. [CrossRef]
16. Lunetta, R.S.; Knight, J.F.; Ediriwickrema, J.; Lyon, J.G.; Worthy, L.D. Land-Cover Change Detection Using Multi-Temporal MODIS NDVI Data. *Remote Sens. Environ.* **2006**, *105*, 142–154. [CrossRef]
17. Shao, Y.; Lunetta, R.S. Comparison of Support Vector Machine, Neural Network, and CART Algorithms for the Land-Cover Classification Using Limited Training Data Points. *ISPRS J. Photogramm. Remote Sens.* **2012**, *70*, 78–87. [CrossRef]
18. Zhu, Z.; Woodcock, C.E.; Olofsson, P. Continuous Monitoring of Forest Disturbance Using All Available Landsat Imagery. *Remote Sens. Environ.* **2012**, *122*, 75–91. [CrossRef]
19. Ren, J.; Shao, Y.; Wan, H.; Xie, Y.; Campos, A. A Two-Step Mapping of Irrigated Corn with Multi-Temporal MODIS and Landsat Analysis Ready Data. *ISPRS J. Photogramm. Remote Sens.* **2021**, *176*, 69–82. [CrossRef]
20. Foody, G.M.; Mathur, A. Toward Intelligent Training of Supervised Image Classifications: Directing Training Data Acquisition for SVM Classification. *Remote Sens. Environ.* **2004**, *93*, 107–117. [CrossRef]
21. Yan, L. Research on LUCC of Huadong Area Based on MODIS. Master's Thesis, Shangdong University of Science and Technology, Qingdao, China, 2011.
22. Friedl, M.A.; Sulla-Menashe, D.; Tan, B.; Schneider, A.; Ramankutty, N.; Sibley, A.; Huang, X. MODIS Collection 5 Global Land Cover: Algorithm Refinements and Characterization of New Datasets. *Remote Sens. Environ.* **2010**, *114*, 168–182. [CrossRef]
23. Belgium, U. *Land Cover CCI Product User Guide Version 2*; University of Catholique de Louvain: Leuve, Belgium, 2016.
24. Kuhn, M. Building Predictive Models in R Using the Caret Package. *J. Stat. Softw.* **2008**, *28*, 1–26. [CrossRef]

25. Ballo, A.; Moustapha, D.; Coulibaly, A. An Application of Machine Learning Methods to Detect Mango Varieties. *Open J. Appl. Sci.* **2024**, *14*, 1666–1690. [CrossRef]
26. Skamarock, C.; Klemp, B.; Dudhia, J.; Gill, O.; Liu, Z.; Berner, J.; Wang, W.; Powers, G.; Duda, G.; Barker, D.M.; et al. *A Description of the Advanced Research WRF Model Version 4*; NCAR Technical Notes, NCAR/TN-556+STR; National Center for Atmospheric Research: Boulder, CO, USA, 2021; pp. 1–3.
27. Thompson, G.; Rasmussen, R.; Manning, K. Explicit Forecasts of Winter Precipitation Using an Improved Bulk Microphysics Scheme. *Part I Descr. Sensit. Analysis. Mon. Weather Rev.* **2004**, *132*, 519–542. [CrossRef]
28. Mlawer, E.J.; Taubman, S.J.; Brown, P.D.; Iacono, M.J.; Clough, S.A. Radiative Transfer for Inhomogeneous Atmospheres: RRTM, a Validated Correlated-k Model for the Longwave. *J. Geophys. Res. Atmos.* **1997**, *102*, 16663–16682. [CrossRef]
29. Dudhia, J. Numerical Study of Convection Observed during the Winter Monsoon Experiment Using a Mesoscale Two-Dimensional Model. *J. Atmos. Sci.* **1989**, *46*, 3077–3107. [CrossRef]
30. Hong, S.-Y.; Noh, Y.; Dudhia, J. A New Vertical Diffusion Package with an Explicit Treatment of Entrainment Processes. *Mon. Weather Rev.* **2006**, *134*, 2318–2341. [CrossRef]
31. Ek, M.B.; Mitchell, K.; Lin, Y.-B.; Rogers, E.; Grunmann, P.J.; Koren, V.; Gayno, G.; Tarpley, D. Implementation of Noah Land-Surface Model Advances in the NCEP Operational Mesoscale Eta Model. *J. Geophys. Res.* **2003**, *108*, 8851. [CrossRef]
32. Li, D.; Bou-Zeid, E.; Barlage, M.; Chen, F.; Smith, J.A. Development and Evaluation of a Mosaic Approach in the WRF-Noah Framework. *J. Geophys. Res. Atmos.* **2013**, *118*, 11918–11935. [CrossRef]
33. Zhu, Q.; Guo, X.; Deng, W.; Shi, S.; Guan, Q.; Zhong, Y.; Zhang, L.; Li, D. Land-Use/Land-Cover Change Detection Based on a Siamese Global Learning Framework for High Spatial Resolution Remote Sensing Imagery. *ISPRS J. Photogramm. Remote Sens.* **2022**, *184*, 63–78. [CrossRef]
34. Loveland, T.; Reed, B.; Brown, J.; Ohlen, D.; Zhu, Z.; Yang, L.; Merchant, J. Development of a Global Land Characteristics Database and IGBP DISCover from 1 Km AVHRR Data. *Int. J. Remote Sens.* **2000**, *21*, 1303–1330. [CrossRef]
35. Hansen, M.C.; Defries, R.S.; Townshend, J.R.G.; Sohlberg, R. Global land cover classification at 1 km spatial resolution using a classification tree approach. *Int. J. Remote Sens.* **2000**, *21*, 1331–1364. [CrossRef]
36. Bartholomé, E.; Belward, A. GLC2000: A New Approach to Global Land Cover Mapping from Earth Observation Data. *Int. J. Remote Sens.* **2005**, *26*, 1959–1977. [CrossRef]
37. Bontemps, S.; Defourny, P.; Bogaert, E.V.; Arino, O.; Kalogirou, V.; Perez, J.R. *Globcover 2009-Products Description and Validation Report*; University of Catholique de Louvain: Leuve, Belgium, 2011.
38. Friedl, M.; Sulla Menashe, D. *Note to Users of MODIS Land Cover (MCD12Q1) Products Report*; NASA: Washington, DC, USA, 2011.
39. Chen, J.; Chen, J.; Liao, A.; Cao, X.; Chen, L.; Chen, X.; He, C.; Han, G.; Peng, S.; Lu, M.; et al. Global Land Cover Mapping at 30m Resolution: A POK-Based Operational Approach. *ISPRS J. Photogramm. Remote Sens.* **2015**, *103*, 7–27. [CrossRef]
40. Hansen, M.C.; Potapov, P.; Moore, R.; Hancher, M.; Turubanova, S.; Tyukavina, A.; Thau, D.; Stehman, S.; Goetz, S.; Loveland, T.; et al. High-Resolution Global Maps of 21st-Century Forest Cover Change. *Science* **2013**, *342*, 850–853. [CrossRef] [PubMed]
41. López-Espinoza, E.; Zavala-Hidalgo, J.; Mahmood, R.; Ramos, O. Assessing the Impact of Land Use and Land Cover Data Representation on Weather Forecast Quality: A Case Study in Central Mexico. *Atmosphere* **2020**, *11*, 1242. [CrossRef]
42. Du, J.; Xu, X.; Liu, H.; Wang, L.; Cui, B. Deriving a High-Quality Daily Dataset of Large-Pan Evaporation over China Using a Hybrid Model. *Water Res.* **2023**, *238*, 120005. [CrossRef]
43. Belgiu, M.; Drăguţ, L. Random Forest in Remote Sensing: A Review of Applications and Future Directions. *ISPRS J. Photogramm. Remote Sens.* **2016**, *114*, 24–31. [CrossRef]
44. Fassnacht, F.E.; Latifi, H.; Stereńczak, K.; Modzelewska, A.; Lefsky, M.; Waser, L.T.; Straub, C.; Ghosh, A. Review of Studies on Tree Species Classification from Remotely Sensed Data. *Remote Sens. Environ.* **2016**, *186*, 64–87. [CrossRef]
45. Kutz, K.; Cook, Z.; Linderman, M. Object Based Classification of a Riparian Environment Using Ultra-High Resolution Imagery, Hierarchical Landcover Structures, and Image Texture. *Sci. Rep.* **2022**, *12*, 11291. [CrossRef]